Real-time passive monitoring with a fibre-optic ocean bottom array

Alex Goertz[1*] and Andreas Wuestefeld[2] discuss the value of real-time seismic monitoring in offshore oilfields and present results from a fibreoptic pilot installation in a Norwegian fjord.

Introduction

To achieve high recovery rates, modern-day production management can benefit from not only snapshot images of the state of the reservoir at regular time intervals, but also continuous monitoring of the dynamic processes induced by pressure changes and fluid movement during production. Production management using time-lapse 4D snapshots is reactive, i.e., adjustments addressing the sweep efficiency or reservoir integrity can only be instigated once the next snapshot image is available after acquisition, processing and interpretation, often years later. For a more proactive reservoir management, it is important to have dynamic reservoir information in real time between the seismic time-lapse snapshots. Such information is contained in microseismic monitoring data and in surface or borehole deformation measurements. If sensors are permanently installed, this information comes at a negligible additional cost, provided that the data can be transferred to shore in real-time and processed automatically.

Time-lapse 4D snapshot images are typically obtained over a period of years and are inadequately sampled for capturing dynamic reservoir changes taking place over much shorter time intervals, from hours to days. Such changes can include variations in the permeability caused by scaling or compaction (Barkved and Kristiansen, 2005), changes of the fluid phase owing to pressure variations (e.g., Osdal et al., 2006), unintended alterations of the flow paths owing to out-of-zone injections and fault reactivation (e.g., Schinelli et al., 2015), or movement in the overburden, potentially compromising the integrity of infrastructure in the form of casing failures or seafloor subsidence (e.g., Yudovich et al., 1989; Hatchell et al., 2017). While 4D seismic data can capture the cumulative effect of such processes by evaluating differences in still images every few years, they provide little information about when exactly the associated dynamic changes occurred and how they relate to changes in flow rate and pressure that may have been captured through continuous measurements in the wellbores accessing the reservoir.

Microseismic events from within or around a producing reservoir can be indicative of reservoir fluid pathways and sub-seismic reservoir compartmentalization (e.g., Maxwell and Urbancic, 2001), or stress changes and associated production-related deformations in the vicinity (e.g., Teanby et al., 2004; Zoback and Zinke, 2002; Wuestefeld et al., 2011, 2013). Continuous monitoring of seismicity can also help in assessing deformation-related risks to infrastructure over the life of a field. Combined with pressure and flow rate, such data can provide the necessary information to capture dynamic processes in the reservoir right when they happen. In conjunction with geomechanical flow modelling, production optimization strategies can thus be validated and adjustments can be properly planned at an early stage. The result will be an improved sweep efficiency with a further increased recovery factor, as well as better risk assessment with the avoidance of potentially costly mitigation actions. A better understanding of, and continuous information about, the reservoir dynamics may even help to plan a 4D seismic strategy better. This can include better definition of suitable intervals for the acquisition of time-lapse images. These intervals could be irregular, depending on the state of reservoir development and type of recovery method. Continuous monitoring may also provide a means to high-grade areas of the reservoir for partial 4D imaging at lower cost and faster turnaround in between 'full' time-lapse surveys (Hatchell et al., 2013).

In this paper we discuss the general ability to monitor microseismic events in an offshore setting and presents results from a real-time monitoring pilot in Norway. We validate the concept of continuous real-time monitoring from a fibre-optic deep-water installation by comparing our automatic detections with data from a regional seismograph network.

Real-time pilot installation in Sognefjord

In June 2017, the latest version of PGS' OptoSeis fiberoptic PRM system was installed in Sognefjord, the longest and deepest of all Norwegian fjords. This location was selected for its unique combination of easy access to onshore facilities (for both, physical maintenance, and remote connectivity), and the possibility it offered for deploying sensor cables in deep water over an extended time period. Such water depths are found in the fjords of coastal Norway, but not farther out on the shelf. Two cables were deployed side-by-side with 68 four-component (three orthogonal accelerometers plus hydrophone) sensor nodes in total. The fiberoptic cable system consists of pressure-balanced passive sensors which are interrogated from a topside unit (see Goertz et al., 2017 for further details). The sensors are placed in the deepest part of the fjord at a water depth of 1300 m, and not buried. The fjord bottom consists of clay-rich quaternary sediments. Figure 1 shows an aerial overview of the installation location. The position

[1] PGS | [2] NORSAR
[*] Corresponding author, E-mail: alexander.goertz@gmail.com

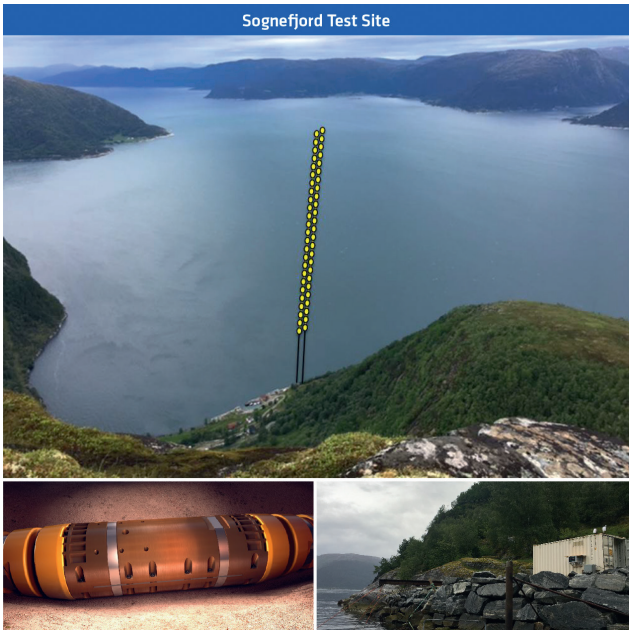

Figure 1 Overview of the test site in Sognefjord, Norway. Approximate location of subsea cables & sensors is indicated in yellow. The recording equipment is located in a 20' container onshore (lower right). Each seafloor sensor station (lower left) consists of a hydrophone and a three-axis accelerometer. Water depth is about 1300 m.

of the cables and sensors is approximately indicated. The cables are tied off at the shore where optical interrogation and data pre-processing equipment is located in a 20-ft container (depicted at the bottom right of Figure 1). Here, data is continuously recorded, packaged into suitable chunks and automatically transferred to the PGS office in Oslo for further analysis. With a 4 ms sampling rate, the array produces about 1 GB of data per hour. Depending on the choice of recording parameters and processing workflow, the system can record real-time with a latency (to a workstation in the office) of about 40-120 sec. The continuous data was scanned automatically for earthquake signals using an STA/LTA approach, with only minimum human intervention for quality control. Figure 2 depicts a flow diagram for real-time monitoring with the pilot array. Depending on the application, results from such monitoring systems can be available within minutes or hours for decision making. Examples include monitoring the effectiveness of completions in onshore fracking operations, the detection of seafloor leakages of mud re-injections (Dando et al., 2016), or traffic-light systems for monitoring induced seismicity (Kao et al., 2018).

Different recording parameters are often necessary for continuous passive monitoring and for active source time-lapse imaging with the same array. This can include different array configurations and sampling rates. It is therefore necessary to be able to quickly change recording parameters remotely between passive monitoring and active seismic imaging. Sometimes, field operations may warrant focusing the monitoring (or imaging) on a particular portion of the field, e.g., a recently drilled injector. The system can therefore be fully remotely operated. Recording parameters, such as the configuration of active stations, can be modified remotely.

Passive monitoring in noisy offshore environments

Onshore unconventional shale plays were the main driver for the development of microseismic monitoring over the last decade (Duncan and Eisner, 2010; Maxwell et al., 2010; Wuestefeld et al., 2012). Offshore, however, passive seismic methods are much less established, despite the fact that offshore applications were the first to validate the methodology in the E&P industry (Maxwell and Urbancic, 2001; Dyer et al., 1999). The reasons for this are multifold: On the one hand, the uncertainties of microseismic detection and location were large and the understanding of associated subsurface processes in conventional fields were limited, therefore a valid business case was not always obvious. In addition, it can prove challenging and costly to install seismic sensors offshore (whether on the seafloor or in an offshore well) owing to the inaccessibility, and the ambient noise level can be comparatively high.

The value proposition for passive monitoring offshore has become clearer in recent years: Firstly, improvements in microseismic monitoring techniques have reduced uncertainties and ambiguities. Noteworthy are improvements in array processing technology and associated sensor configurations (Pesicek et al., 2014; Grechka et al., 2015, 2016; Bussat et al., 2016), more appropriate consideration of the underlying physics by using three-component data and consideration of the elastic wave field (Artman et al., 2009), or anisotropy (Grechka et al., 2015). Secondly, reservoir simulations can model the underlying

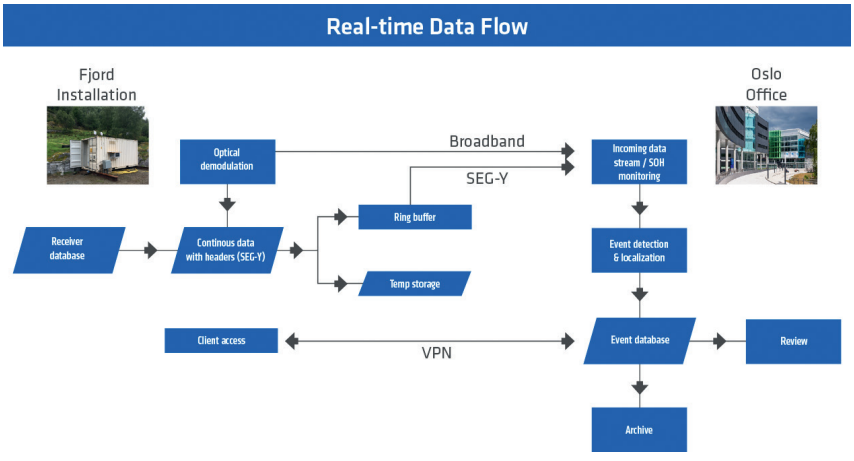

Figure 2 Flow diagram for real-time flow of data and status updates from the remote recording site (in this case the fjord) to the processing centre or the client's desktop.

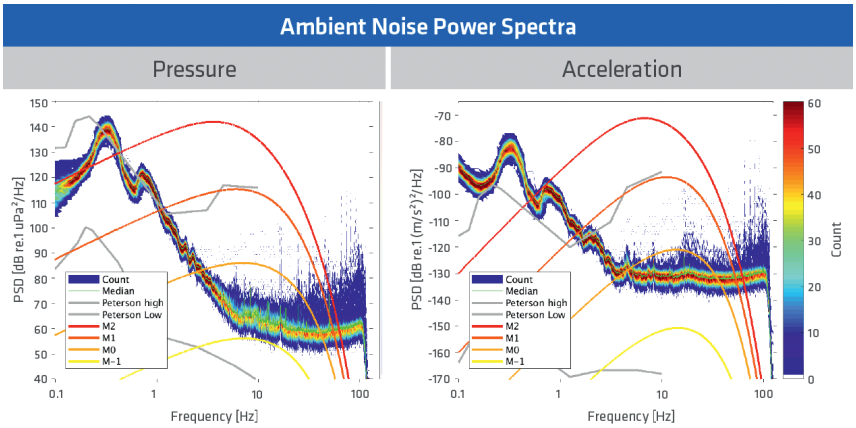

Figure 3 Ambient noise power spectra and their variation over a 10 h time period for a hydrophone (left) and accelerometer (right) recording compared to expected power spectra of regional earthquakes of various magnitude. See text for explanation.

deformation processes more accurately nowadays through the use of fully coupled geomechanical flow modelling (e.g., Herwanger et al., 2016; Oppert et al., 2017).

Offshore challenges include sensor installation (although fiberoptic technology reduces per-channel costs in principle), and the very different and often higher noise level offshore. We illustrate the latter in more detail in Figure 3 which shows noise power spectra from a sensor of the Sognefjord pilot array at 1300 m water depth. Since noise is inherently non-stationary, we need to evaluate the power spectral density distribution over a time period in order to get a good estimate. We calculate power spectra for ten consecutive hours (midnight to 10 am) using a multi taper method (Park et al., 1987) over a sliding 2 min window without overlap. The resulting spectra are amplitude binned as a histogram for each frequency sample and colour-coded by number of occurrence (McNamara & Buland, 2004). Warm colours denote the mode of the distribution, and cold colours indicate the variability of the power spectral density over the analysed time period. Note, that below 10 Hz the noise level is high, but stable with little variation (< 10 dB). The pronounced peak at about 0.2 Hz is caused by the so-called secondary ocean microseism. Seismologists noted early on (Gutenberg, 1912) that strong ocean microseisms appeared to originate from the coast of western Norway. Consequently, we observe in our measurements a noise level at this frequency range consistently around or even above the expected global average high noise level according to the model of Peterson (1993; gray lines in Figure 3).

At higher frequencies, the ambient noise level declines steeply by at least 50 dB with similarly small variability until the spectra flatten out between 5 to 10 Hz where we observe an increase of the variability in the form of a wider spread of blue colours. Here we enter the realm of anthropogenic noise, a non-stationary cacophony of mostly transient signals caused by traffic, industry and other sources. We attribute the bulk of the variability observed in our data to sporadic ship traffic. However, anthropogenic noise levels are overall comparatively low owing to the remote location of the sensor array. The area is sparsely populated, especially during the winter months (recording is from December 2017). We also note that the distribution of power spectral levels at higher frequencies is skewed with less variance towards the low side, and particularly for the accelerometer is more or less flat. This is an indication that we are close to the instrument noise limit at these spectral levels.

The sensitivity of an optical sensor can in principle be chosen freely, but is in practice a function of the expected dynamic range of the signal. The desired upper end is given by the maximum expected active source signal (typically an airgun array) to reach the sensor. Sensor sensitivities are often chosen as a function water depth: the deeper the water, the further the sensor is away from the active source, thus the higher its sensitivity can be. Similar to an electrical system, the sensitivity of an optical sensor is in general a function of the reaction mass, the spring stiffness, and the length of optical fibre in it. If no good compromise can be found for the sensor specification to cover the desired dynamic range, one solution could be to package sensors of different sensitivity into the same housing. It should be noted however, that seafloor ambient noise levels in an offshore oil field are typically higher than what we observe here in our secluded spot in the fjord (see, e.g., Bjerrum et al., 2014), and hence above the sensor noise floor of this particular embodiment.

In order to judge the sensitivity of our array to micro earthquakes, we compare the measured noise levels to expected earthquake source spectra using the model of Brune (1970), scaled to seismic moment according to Boatwright (1984). The effect of the travel path is considered by multiplying the spectra with a factor of $e^{-\frac{\pi f t}{Q}}$, where t denotes the travel path and Q the attenuation factor. The resulting spectra are shown as red-to-yellow curves in Figure 3 for various moment magnitudes. Since we expect mostly regional tectonic earthquakes in the vicinity of our array, we use an average distance of 20 km and a Q-factor of 200. Thus, judging from Figure 3, the array should be capable of detecting earthquakes as low as magnitude (M) 0 and below from a distance of 20 km. When discussing magnitude, we typically refer to the moment magnitude (M_W). It should, however, be noted that for an unbiased estimate of the event's moment magnitude, the linear low-frequency part of the source spectrum, in this case below 1-5 Hz, should be captured with sufficient signal-to-noise. Owing to the strong increase of the ambient noise level at these frequencies, accurate magnitude determinations will be difficult with ocean bottom sensors.

Data examples

We present here results from about one month of coninuous data from the Sognefjord array. We compare our detections with the NORSAR catalogue of tectonic events (see www.jordskjelv.no, in Norwegian). An overview of these matching events is shown in

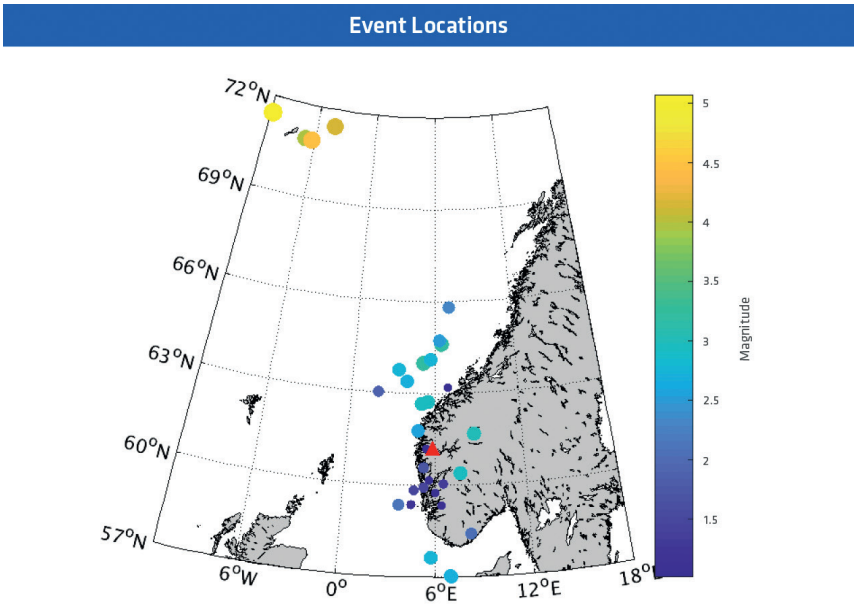

Figure 4 NORSAR catalogue locations of events detected by the Sognefjord array (shown with a red triangle) during December 2017. The largest events in this time period occurred on the Mid-Atlantic Ridge near the island of Jan Mayen. Local events can include tectonic events and quarry blasts.

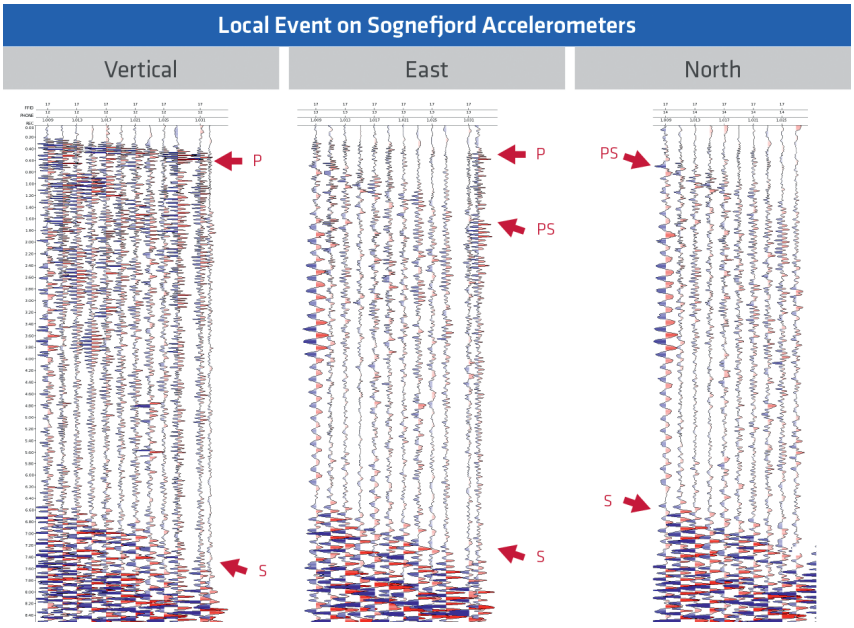

Figure 5 Example recording of a local M1 event about 20 km away. A 3 Hz lowcut filter was applied. Left panel shows the vertical component of acceleration, and the middle and right panel the east and north component respectively. We note clear P- and S arrivals as well as a local P to S conversion at the basement under the array.

Figure 4. The largest event recorded during the analysed period was a M5 earthquake near the island of Jan Mayen, located on the Mid-Atlantic Ridge. Several local events of around M1 were recorded. One example record of a Magnitude 1 event at about 20 km distance is shown in Figure 5. We show accelerometer data for one of the two cables located in the flat part of the bottom of the fjord situated on sediments. To limit the amount of data handling for this pilot, only every second sensor was active during the continuous monitoring period. These sensors are roughly spaced 100 m apart over an array length of 1 200 m. Components were rotated to vertical, east and north respectively, using active source calibration data acquired at the time of deployment. Note the clear P and S arrivals, with the shear wave arrival exhibiting stronger amplitudes and lower frequencies. In addition, a secondary phase is observed on the horizontal components. We interpret this as a P to S conversion originating from the basement under the array (red arrows in Figure 5). The strong velocity contrast between granitic basement and quarternary sediment gives rise to strong mode conversions.

Since the sediment cover under the array thickens from south to north (left to right in the record), the P-S conversion shows a differential moveout compared to the P arrival. This is illustrated in more detail in Figure 6, where we zoom on to the P arrival and plot the hydrophone components in addition. The hydrophones are shown as black traces and offset from their respective collocated 3C accelerometer counterparts for better visibility. The topmost four stations are located on the fjord wall on hard rock, and no local P-S conversion can be discerned in the arrival. As the sensor locations approach the sedimentary infill at the fjord bottom, we note a P-S converted phase on the horizontal components which separates increasingly from the P arrival (best seen on the hydrophones in this display), reflecting the thickening sediment away from the fjord wall toward the centre. We also note a free-surface multiple (denoted in

seismological terms as pP) on the hydrophone channels, about 1.7 s after the first arrival.

Microseismic detectability in offshore oilfields

Having shown an example of continuous passive monitoring, we now attempt to translate the findings to oilfield monitoring applications. Compared to tectonic events (majority of events recorded on the Sognefjord pilot installation), production-induced microseismicity shows some different characteristics. On one hand, the potential target volume for microseismic events would be closer to the array, at typical distances of a few kilometres, but on the other hand, production-induced seismicity consists of much smaller events. In fact, part of the objective is sometimes to capture small events to anticipate and ultimately prevent larger deformations. We therefore recalculate the Brune source spectra shown in Figure 3 for the case of production-induced seismicity at typical reservoir depths (2.5 km) in sedimentary basins with a lower quality factor (Q) of 50, shown in Figure 7a.

Since noise levels vary with time, we assess the detectability probabilistically. We expand the method presented by Goertz et al. (2012) and compare the various percentiles of the quasi-stationary noise distribution with the expected signal levels for various magnitudes. We divide the integrated microseismic signal level S for each magnitude over the integrated noise level N_p for each percentile of the distribution,

$$\frac{S}{N} = \frac{\int_{f_0}^{f_1} S(f)df}{\int_{f_0}^{f_1} N_P(f)df}$$

where the subscript P denotes the respective percentile of the noise distribution. The result, shown in Figure 7b, is a signal-to-noise ratio as a function of magnitude and noise percentile of the assumed quasi-stationary noise distribution, in this case coming from our measurement in the pilot array. If we assume that we can reliably detect a microseismic event with a signal-to-noise ratio of 1 using array processing techniques, a contour line at this ratio (dashed line in Figure 7b), gives the cumulative probability of detecting an earthquake of specified magnitude. For example, an event of M-0.8 would be detected with 50% probability, and event of M-0.5 would almost always be detected, and at M-1.5, only about 10% of events would be detected. In the presented case, we analyse a frequency range of 1 to 100 Hz, the upper end limited by the sampling rate of the underlying noise measurement. We note however from Figure 7a that higher frequencies are expected to contribute to the microseismic signal. The method does not take into account any coherent noise suppression methods (Dando et al., 2016), or the possibility of enhancing detectability with array stacking methods. Furthermore, we only assess the detectability of P arrivals on one component. It can be shown that the use of all

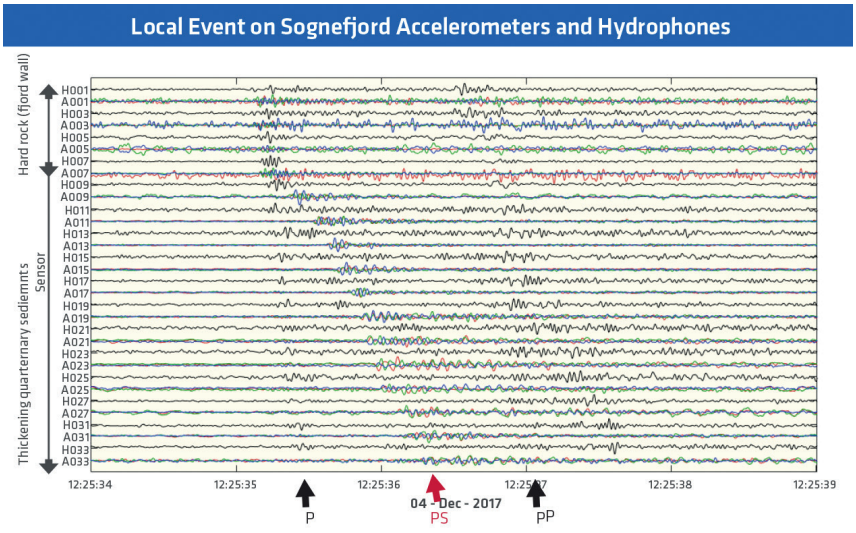

Figure 6 P arrival from the event in Figure 5, with additional display of the hydrophone components (in black and for visibility offset from the coloured three-component accelerometer traces), and additional stations located on hard rock of the fjord wall. 3 Hz low-cut filter applied.

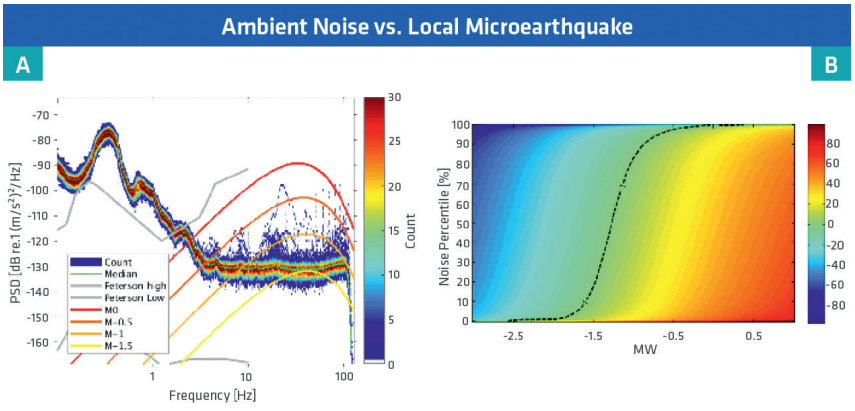

Figure 7 a) Ambient noise power spectral distribution shown in comparison to expected source spectra of reservoir microseismicity at a depth of 2.5 km with an average Q of 50. Detection threshold shifts to lower magnitudes and higher frequencies. b) Probabilistic detectability as a function of magnitude and noise percentile for the situation depicted on the left. Colour denotes signal-to-noise ratio in dB. Dashed black curve shows detection probability for a SNR of 1.

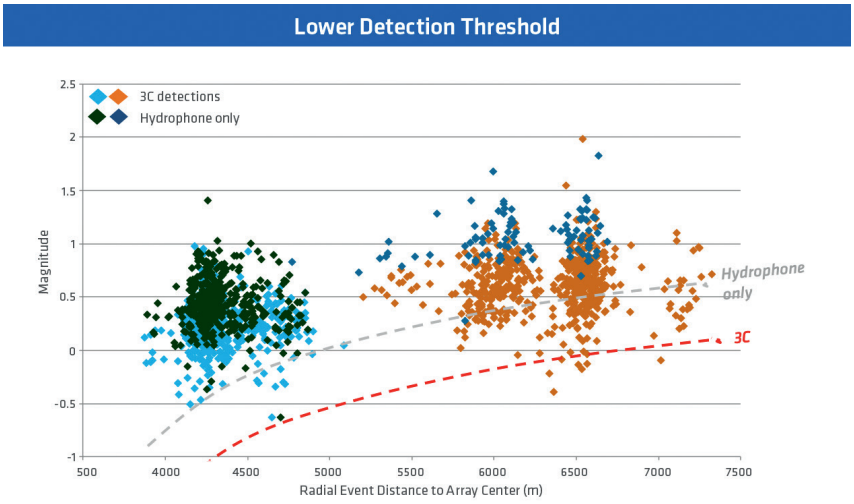

Figure 8 Magnitude of detected events as a function of distance from the array from a passive monitoring campaign in Brazil. The same data was analysed using only the hydrophone component and using three-component recordings. Using three-component data results in significantly more detections, particularly at lower magnitudes, hence lowering the detection threshold by 0.5 magnitude units (grey and red dashed lines).

three components and stronger shear wave arrivals (Witten et al., 2012) can significantly lower the detection threshold.

Figure 8 shows an example from passive monitoring at a PRM installation offshore Brazil (Ramos Filho et al., 2017). Here, moment magnitude is plotted versus distance. Dark green and blue colours indicate events detected using only hydrophone data, whereas cyan and orange colours denote events detected using all four components. The detection threshold changes as a function of distance owing to geometrical spreading and inelastic attenuation (grey and red dashed lines in Figure 8). By using all four components the detection threshold can be lowered by about 0.5 magnitude units compared to using only hydrophone data. This is a result of a combination of significant signal energy visible as shear waves on the horizontal components, and lower acoustic noise levels on the accelerometers.

Conclusion

Recovery factors from offshore reservoirs can be increased further through continuous real-time passive seismic monitoring in between time-lapse snapshot images. Real-time microseismic monitoring can immediately reveal dynamic reservoir processes and significantly shorten the decision cycles for reservoir management, thus complementing 4D time-lapse data acquisitions. Microseismic events reveal the time history of deformations and can provide valuable constraints for history matching of coupled geomechanical and reservoir flow models. Using such data for continuous proactive reservoir management can therefore optimize sweep efficiency and mitigate risk. Our test of performing automatic event detection on data from a fiberoptic pilot installation in Sognefjord and comparison with catalogue data from the Norwegian regional seismic network proves the concept of real-time monitoring and remote operation of an ocean bottom sensor array. We use the measured noise levels to perform a probabilistic estimate of microseismic detection thresholds for an ocean-bottom PRM installation. These outcomes are encouraging for future offshore arrays to capture the microseismic reservoir response. We conclude that with optimal design of a monitoring network and the use of array processing methodology it should be possible to detect a sufficient number of events with an ocean bottom sensor array to provide meaningful input for reservoir characterization. In conjunction with good estimates of the expected deformation from geomechanical and flow modelling, microseismic results are a relevant value addition for offshore conventional reservoir management.

Acknowledgements

We are grateful to PGS for the permission to publish the results presented herein. We would also like to thank Julien Oukili for help with processing of some of the data, and Vinnie Papenfuss for help with the figures. Edits by Aoife O'Mongain, and Andrew Long helped to improve the manuscript.

References

Artman, B., Podladtchikov, I. and Goertz, A. [2009]. Elastic time-reverse modeling imaging conditions. *79th Technical Program, SEG*, Expanded Abstracts, 1207-1211, doi:10.1190/1.3255069.

Auger, E., Schisselé-Rebel, E. and J. Jia [2013]. Suppressing noise while preserving signal for surface microseismic monitoring: The case for the patch design. *83rd Technical Program, SEG*, Expanded Abstracts, 2024-2028, doi:10.1190/segam2013-1396.1.

Barkved, O. and T. Kristiansen [2005]. Seismic time-lapse effects and stress changes: Examples from a compacting reservoir. *The Leading Edge,* **24** (12), 1244-1248, doi:10.1190/1.2149636

Bjerrum, L., Matveeva, T., Lindgård, J., Rutledal, H. and Yde, A., 2014, Comparison of Noise Characteristics on an Untrenched and Trenched Cable Deployed in the North Sea for a PRM System, *76th EAGE Conference & Exhibition*, Expanded Abstracts, We E103 03.

Boatwright, J. [1984]. Seismic estimates of stress release. *Journal of Geophysical Research*, **89**, 6961–6968.

Brune, J. [1970]. Tectonic stress and the spectra of seismic shear waves from earthquakes. *Journal of Geophysical Research*, **75**, 4997–5009.

Bussat, S., Bjerrum, L., Dando, B., Bergfjord, E., Iranpour, K. and V. Oye [2016]. Offshore injection and overburden surveillance using real-time passive seismic. *First Break*, **34** (7), 51 – 59.

Caley, A., Kendall, J.-M., Jones, R., Barkved, O., and P. Folstad [2001]. Monitoring fractures in 4D using microseismic data. *63rd EAGE Conference & Exhibition*, Extended Abstracts, F-23.

Dando, B., Iranpour, K., Oye, V., Bussat, S. and L. Bjerrum [2016]. Real-time microseismic monitoring in the North Sea with advanced noise

removal methods. *86th Technical Program, SEG*, Expanded Abstracts, 2657-2661, doi:10.1190/segam2016-13840150.1.

Duncan, P. and L. Eisner [2010]. Reservoir characterization using surface microseismic monitoring. *Geophysics*, **75** (5), 75A139-75A146. doi:10.1190/1.3467760.

Dyer, B., R. Jones, J. Cowles, O. Barkved and P. Folstad, [1999]. Microseismic Survey of a North Sea Reservoir. *World Oil*, (March), 74-78.

Goertz, A., Smith, A. and D. Lecerf [2017]. Maximize value with efficient next-generation fiberoptic monitoring solutions. *First EAGE Workshop on Practical Reservoir Monitoring,* doi: 10.3997/2214-4609.201700015.

Goertz, A., Riahi, N., Kraft, T. and M. Lambert [2012]. Modeling detection thresholds of microseismic monitoring networks. *82nd Technical Program, SEG*, Expanded Abstracts, doi: 10.1190/segam2012-1069.1.

Grechka, V., De La Pena, A., Schisselé-Rebel, E., Auger, E. and P. Roux [2015]. Relative location of microseismicity. *Geophysics*, **80** (6), WC1-WC9, doi:10.1190/geo2014-0617.1.

Grechka, V., Li, Z., Howell, B. and V. Vavryčuk [2016]. Single-well moment tensor inversion of tensile microseismic events. *Geophysics*, **81** (6), KS219-KS229, doi:10.1190/geo2016-0186.1.

Grechka, V. [2015]. Tilted TI models in surface microseismic monitoring. *Geophysics*, **80** (6), WC11-WC23, doi:10.1190/geo2014-0523.1.

Gutenberg, B. [1912]. Die seismische Bodenunruhe. *Gerl. Beitr. Geoph.*, **11**, 314.

Hatchell, P., Wang, K., Lopez, J., Stammeijer, J. and M. Davidson [2013]. Instantaneous 4D seismic (i4D) for offshore water injection monitoring. *83rd Technical Program, SEG*, Expanded Abstracts, 4885-4889, doi: 10.1190/segam2013-0444.1.

Hatchell, P., R. de Vries, V. Gee, H. Cousson, J. Lopez, S. Dunn, N. Street, A. Parsons, J. Cheramie, and E. Fischer [2017]. Seafloor deformation monitoring: Past, present, and future. *87th Technical Program, SEG*, Expanded Abstracts, 5233-5238, doi: 10.1190/segam2017-17722686.1.

Herwanger, J, Bottrill, A. and P. Popov [2016]. One 4D geomechanical model and its many applications. *78th EAGE Conference & Exhibition*, Extended Abstracts, Th LHR5 13.

Kao, H., Visser, R., Smith, B. and S. Venables [2018]. Performance assessment of the induced seismicity traffic light protocol for northeastern British Columbia and western Alberta. *The Leading Edge*, **37** (2), 117–126, doi:10.1190/tle37020117.1.

Maxwell, S.C. and T. Urbancic [2001]. The role of passive microseismic monitoring in the instrumented oil field. *The Leading Edge*, **20** (6), 636–639, doi: 10.1190/1.1439012.

Maxwell, S., J. Rutledge, R. Jones and M. Fehler [2010]. Petroleum reservoir characterization using downhole microseismic monitoring. *Geophysics*, **75** (5), 75A129-75A137, doi: 10.1190/1.3477966.

McNamara, D.E. and R.P. Buland [2004]. Ambient noise levels in the continental United States. *Bulletin of the Seismological Society of America*, **94**, 1517–1527.

Osdal, B., Husby, O., Aronsen, H., Chen, N. and T. Alsos [2006]. Mapping the fluid front and pressure build-up using 4D data on Norne Field. *The Leading Edge*, **25** (9), 1134-1141, doi:10.1190/1.2349818.

Oppert, S., Stefani, J., Eakin, D., Halpert, A., Herwanger, J., Bottrill, A., Popov, P., Tan, L., Artus, V. and M. Oristaglio [2017]. Virtual time-lapse seismic monitoring using fully coupled flow and geomechanical simulations. *The Leading Edge*, **36** (9), 750–768, doi:10.1190/tle36090750.1.

Park, J., Lindberg, C.R. and F.L. Vernon [1987]. Multitaper spectral analysis of high-frequency seismograms. *J. Geophys. Res*., **92** (12),675-12,648.

Peterson, J. [1993]. Observations and modeling of seismic background noise. USGS Open File Report, **95**, 93-322.

Pesicek, J., Child, D., Artman, B. and K. Cieślik [2014]. Picking versus stacking in a modern microearthquake location: Comparison of results from a surface passive seismic monitoring array in Oklahoma. *Geophysics*, **79** (6), KS61-KS68, doi:10.1190/geo2013-0404.1

Ramos Filho, W., Dariva, P., Born, C., Zorzanelli, I., Goertz, A. and A. Smith [2017]. Permanent reservoir monitoring at Jubarte Field - 4D Results and Reservoir Characterization. *First EAGE Workshop on Practical Reservoir Monitoring*, Expanded Abstract.

Schinelli, M., Dabbadia, M., Conners, S., Guerra, R. and A. Kazantsev [2015]. Microseismic technology to monitor fault reactivation. *14th International Congress of the Brazilian Geophysical Society & EXPOGEF*, Expanded Abstracts, 602-604.

Teanby, N., Kendall, J.-M., Jones, R. and O. Barkved [2004]. Stress-induced temporal variations in seismic anisotropy observed in microseismic data. *Geophysical Journal International*, **156**,459–466.

Witten, B., S. Montgomery and B. Artman, 2012, Shear wave arrivals in surface microseismic data. *SEG Technical Program,* Expanded Abstracts, 1-5. doi:10.1190/segam2012-0722.1

Wuestefeld, A., Verdon, J., Kendall, J., Rutledge, J., Clarke, H. and J. Wookey [2011]. Inferring rock fracture evolution during reservoir stimulation from seismic anisotropy. *Geophysics*, **76** (6), WC157-WC166, doi: 10.1190/geo2011-0057.1

Wuestefeld, A., Urbancic, T., Baig., A. and M. Prince [2012]. After a decade of microseismic monitoring: Can we evaluate stimulation effectiveness and design better stimulations. *SPE/EAGE European Unconventional Resources Conference and Exhibition*, SPE152665.

Wuestefeld, A., Urbancic, T. and A. Baig [2013]. Identifying reservoir drainage patterns from microseismic data. *75th EAGE Conference & Exhibition*, Extended Abstracts, doi:10.3997/2214-4609.20130934.

Yudovich, A., Chin, L.Y. and D.R., Morgan [1989]. *Casing Deformation in Ekofisk*. Society of Petroleum Engineers, doi: 10.2118/17856-PA

Zoback, M.D. and C. Zinke [2002]. Production-induced normal faulting in the Valhall and Ekofisk oil fields. *Pure and Applied Geophysics*, **159** (1), 403–420.